An analytical flux density distribution model with a closed-form expression for a flat heliostat

Caitou He[a], Xiaoyue Duan[a], Yuhong Zhao[b,*], Jieqing Feng[a,*]

[a]*State Key Laboratory of CAD&CG, Zhejiang University, Hangzhou, 310058, China*
[b]*Institute of Industrial Process Control, College of Control Science and Engineering, Zhejiang University, Hangzhou, 310027, China*

Abstract

Predicting the flux density distribution on the receiver surface is of significance for designing and deploying a central receiver system. In this paper, an analytical model with a closed-form expression is presented to accurately describe the flux density distribution that a flat heliostat reflects on the receiver plane. The flux spot is modeled as a two dimensional convolution between a uniform light flux density distribution over the heliostat effective reflection surface and a quasi-Cauchy kernel. The convolution is solved analytically as a closed-form expression. The proposed model takes into account the sunlight direction, sun shape, heliostat position, size, orientation, slope error, and shadowing and blocking effects, etc. Extensive experiments and comparisons were conducted, and it shows that the proposed model is more accurate than the prevalent elliptical Gaussian model, in terms of total power and flux density distribution. Due to its closed-form expression, the proposed model can also be efficiently evaluated on a contemporary graphics processing unit to predict the flux spot of a heliostat within 2.8 milliseconds. Thus this model has promising potential in the practical optimization applications.

Keywords: Central receiver system, Convolution, Two dimensional Quasi-Cauchy kernel, Oblique parallel projection, Monte-Carlo ray tracing, Flat heliostat

1. Introduction

Solar thermal power generation through a central receiver system (CRS) is one of the sustainable and environmentally friendly technologies to meet increasing global energy demands (Romero and Steinfeld, 2012; Avila-Marin et al., 2013). The operational strategies of such a system, particularly during unsteady operation states, require intensive transient flux simulation. In addition to the power generation efficiency, the flux density distribution on the receiver surface is also important to ensure system safety (Roldn and Monterreal, 2014). Consequently, an accurate model of the flux spot reflected by a heliostat is of significance to facilitate the tower concept solar energy collection simulation in CRS (García et al., 2008). Further, the flat heliostat and the focusing heliostat are two common types of heliostat deployed in commercial CRS (Osuna et al., 2004; Schell, 2011). The model for the flat heliostat is important because it is the basis to the research of the composite focusing heliostat. It has been investigated by different researchers since the 1970's (Walzel et al., 1977; Elsayed et al., 1995). However, it is nontrivial because the spot is influenced by many factors, such as the heliostat position, size, orientation, slope error, sunlight direction and sun shape (Collado et al., 1986). Shadowing and blocking effects caused by neighbor heliostats should also be thoroughly addressed.

The existing simulation methods can be basically classified into two categories, namely, the ray tracing approach and the analytical approach (García et al., 2008). The ray tracing approach simulates the light energy transition among the sun, heliostat and receiver by sampling and tracing a huge amount of rays discretely. This approach is capable of achieving an accurate prediction of the flux distribution at the cost of high computing complexity. On the other hand, the analytical method describes the flux density distribution with an empirical function, thus decreasing the computing time significantly and has been widely applied in heliostat field layout design (Cruz et al., 2018) and aiming strategy optimization (Wang et al., 2017). In general, the distribution model is represented in terms of a convolution that is related to multiple factors involving the sun, heliostat and receiver. However, a closed-form solution to this convolution is still unknown. The convolution based model is solved either via numerical approximation (Walzel et al., 1977), which is also time consuming, or via model simplifications (Schwarzbözl et al., 2009), which suffers from the loss of simulation accuracy.

To address the problems in the analytical approach, we propose a new flux density distribution model with a closed-form expression to describe the flux spot on a receiver plane that is reflected by a flat heliostat. An imaginary flux density scalar field is first established on the heliostat via a 2D convolution between a uniform flux density distribution function and a quasi-Cauchy kernel, which naturally takes shadowing and blocking effects into account. The convolution is solved as a closed-form expression. Then, the imaginary flux density distribution is projected to the receiver plane through parallel projection. Experiments and comparisons show that the proposed analytical model is accurate; furthermore, it can be efficiently evaluated in parallel on a contemporary GPU due to its closed-form expression. As a result, it will facilitate the flux density distribution simulation and the related optimizations potentially.

The main nomenclature used in this paper is listed as follows:

Nomenclature

- CSRs   circumsolar ratios.

- σ_s standard deviation of the heliostat slope error.

- I_D direct normal irradiance (DNI).

- S_{sub} area of a micro-heliostat surface.

- $\cos w$ heliostat cosine effect.

- ρ heliostat reflectivity.

- η_{aa} atmospheric attenuation factor.

- S_H heliostat surface area.

- $\cos \phi$ receiver plane cosine effect.

- S'_H the projected heliostat surface area on the receiver.

- A the flux density value under ideal mirror reflection assumption.

- IFDSF   imaginary flux density scalar field.

- $\boldsymbol{r}$ reflection direction of the investigated heliostat.

- $\boldsymbol{N}$ heliostat surface normal.

- $\boldsymbol{N}_r$ receiver panel normal.

- $\boldsymbol{o}$ heliostat surface center.

- $\mathbf{I}$ unitary matrix.

- e_{rms} root mean squared error.

- e_{power} flux power error.

- e_{peak} peak error.

The rest of the paper is organized as follows. Section 2 reviews the relevant work on the analytical approach for flux simulation and the sun shape model. Section 3 provides preliminary knowledge. Section 4 briefly describes an improved GPU-implemented ray tracing simulation and its validation; this result is used as the

ground truth for the analytical model derivation. Section 5 analyzes the modeling process from a theoretical point of view. Section 6 elaborates the derivation of the analytical model and presents a parameter optimization method. Section 7 describes extensive experiments and comparisons with other related works. Section 8 draws conclusions and discusses planned future work.

2. Related work

2.1. Analytical models for the flux density distribution simulation

An analytical approach is one possible way to simulate the received flux density distribution on a receiver reflected by a heliostat, which takes multiple factors into account, such as the sun parameters, heliostat properties and atmospheric attenuation.

Biggs and Vittitoe (1976) proposed statistically incorporating the effects of several nondeterministic factors (e.g., sun tracking errors and facet-surface errors) through a convolution that is solved numerically by using Fourier transformation. Walzel et al. (1977) predicted the flux density distribution on the receiver reflected by a flat heliostat statistically by using a 2D Hermite function. The results are consistent with those generated by previous analytical models but only take about one tenth of the computing time. Lipps and Walzel (1978) proposed an analytical model for a round heliostat and a numerical method to describe the flux density distribution of a heliostat of arbitrary shape, which considers shadowing and blocking effects. The authors indicated that their method was less efficient but more accurate than the Hermite function method (Walzel et al., 1977). Hennet and Abatut (1984) derived a complex analytical flux density distribution model by solving the convolution over the intersection area between the solar disc and the principal image of a heliostat on the receiver. The shadowing effect was handled in a straightforward manner by uniformly decreasing the reflected power according to the percentage of the shadowed area on the heliostat, which is not accurate enough for flux density distribution prediction. Collado et al. (1986) presented the UNIZAR model in the integral form to describe the flux density distribution on the receiver reflected by a focusing heliostat, which is the convolution of several Gaussian distributions. They verified the analytical model by comparing simulated isoflux contours and the total power with practical measurement results. In summary, a general and closed-form solution to the above convolution approaches for flux density distribution simulation is still unknown.

Elsayed et al. (1995) measured the flux density distribution on a planar receiver reflected by a flat heliostat. They identified two images (namely, an apparent image and a mirrored reflected-radiation image) based on the measured data, which turned out to be quite consistent with the results of our analytical model. The flux data was regularly distributed along the primary axes of the principal image (the oblique projection of the mirror surface on the receiver plane). A 1D analytical model (Elsayed and Fathalah, 1994) considering shadowing and blocking effects was given and validated against the measurements (Elsayed et al., 1995).

As an alternative, the convolution-based analytical model can be simplified as a closed-form expression, which may sacrifice the accuracy of the model to some extent. Schwarzbözl et al. (2009) approximated the flux distribution on the receiver surface with a circular Gaussian distribution, namely, the HFLCAL model. The attributes regarding the sun shape, mirror slope errors and tracking errors were parameterized as the deviations of the Gaussian model, which was then verified by comparison with measured data (Collado, 2010). The model was then applied to heliostat-aiming optimization (Salomé et al., 2013; Besarati et al., 2014). García et al. (2015) refined the HFLCAL model by first modeling the reflected flux density as a circular normal distribution on the heliostat and then projecting it to the planar receiver through the homography transformation, i.e., oblique parallel projection. Such projection more closely approximates the distorted flux spot in the real scene and thus leads to a more accurate representation. Huang and Sun (2016) proposed modeling the flux density distribution by a focusing heliostat with an elliptical Gaussian distribution. Shadowing and blocking effects

were not considered. Based on the HFLCAL model, He et al. (2017) proposed a fast simulation method for flux density prediction on the receiver by exploiting the parallel computing and rendering capability of modern GPUs, taking both shadowing and blocking effects into consideration. Due to the flux density distribution model adopted and the characteristics of the z-buffering algorithm (Catmull, 1974; Kessenich et al., 2016), the flux distribution along the silhouettes of the blocked or shadowed areas is sharp, which is inconsistent with actual observations. To overcome this problem, a new model considering both shadowing and blocking effects merits investigation.

2.2. Sun shape model

The sun shape model is essential for accurate flux density distribution analysis, which describes the terrestrial brightness distributions of the sun. In contrast, the direct normal irradiance (DNI) is a general measurement of the solar irradiance reaching a surface perpendicular to the sunlight direction. A simple profile, e.g., the pillbox distribution (Biggs and Vittitoe, 1976) or the Gaussian distribution (Bendt and Rabl, 1981) provides only a rough approximation of the sun shape. Based on the measured data, Neumann et al. (2002) presented several sun shape profiles corresponding to different circumsolar ratios (CSRs), which are the ratios of the solar power hosted by the solar aureole to the total energy emitted from the sun. Based on their work, Buie et al. (2003) proposed an empirical model to describe the relationship between the normalized solar intensity ($S(\theta)$) and the angular displacement from the center of the sun:

$$S(\theta) = \begin{cases} \dfrac{\cos(0.326\theta)}{\cos(0.308\theta)}, & \{\theta \in R | 0 \leq \theta \leq 4.65 \text{ mrad}\} \\ e^{\kappa}\theta^{\gamma}, & \{\theta \in R | \theta > 4.65 \text{ mrad}\} \end{cases} \tag{1}$$

$$\gamma = 2.2\ln(0.52\chi)\chi^{0.43} - 0.1, \quad \kappa = 0.9\ln(13.5\chi)\chi^{-0.3}, \quad \chi = CSR,$$

which agrees well with the measurements at various sites and has been widely adopted in ray tracing simulations. An illustration of Buie's model is shown in Figure 1.
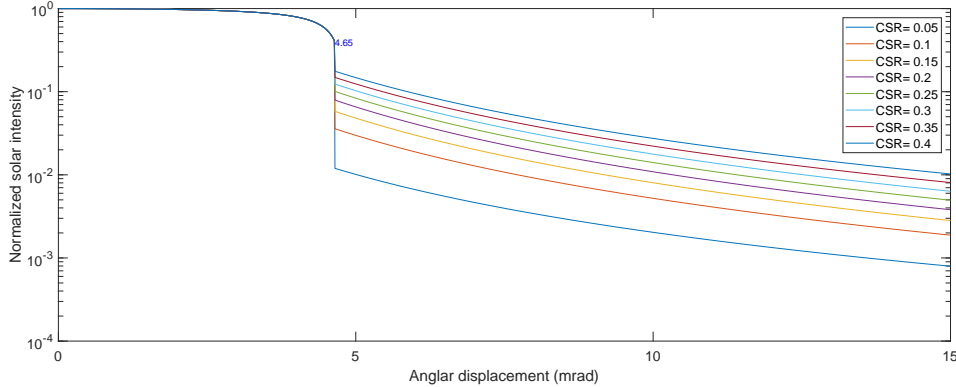

Figure 1: Sun shape model proposed by Buie et al. (2003)

3. Preliminary knowledge

In this section, we briefly introduce preliminary knowledge used in the derivation of the proposed model. This includes the definition of various coordinate systems, the Weiler-Atherton clipping algorithm for shadowing

or blocking area extraction, the Green theorem for converting a 2D double integral into 1D line integrals and a quasi-Cauchy kernel for smooth transition of the flux density distribution.

3.1. Coordinate systems

To describe the heliostat field and the receiver in the CRS, three coordinate systems are defined, namely, the global coordinate system, heliostat coordinate system and receiver plane coordinate system, as shown in Figure 2:

Global coordinate system $O\text{-}XYZ$. This is a 3D Cartesian coordinate system describing the scene of the heliostat field and receiver. Its origin is at the center of the tower base; the X-axis and Z-axis point to the east and the north, respectively, and the Y-axis is vertical to the ground. It is left-handed, which is consistent with the graphics API adopted, i.e., Direct3D (Coordinate Systems (Direct3D)). The azimuth of the sun is defined clockwise from east in degrees and the elevation is defined upwards from the horizon.

Heliostat coordinate system $o\text{-}xy$. This is a 2D coordinate system used to describe a heliostat. Its origin o is at the center of the heliostat surface, and its x-axis is parallel to the long edge of the heliostat.

Receiver plane coordinate system $c\text{-}uv$. This is a 2D coordinate system for describing a planar receiver locally. Its origin c is at the receiver panel center, and the u-axis is parallel to the ground. If the receiver is composed of several planar panels, a receiver plane coordinate system is defined for each panel.
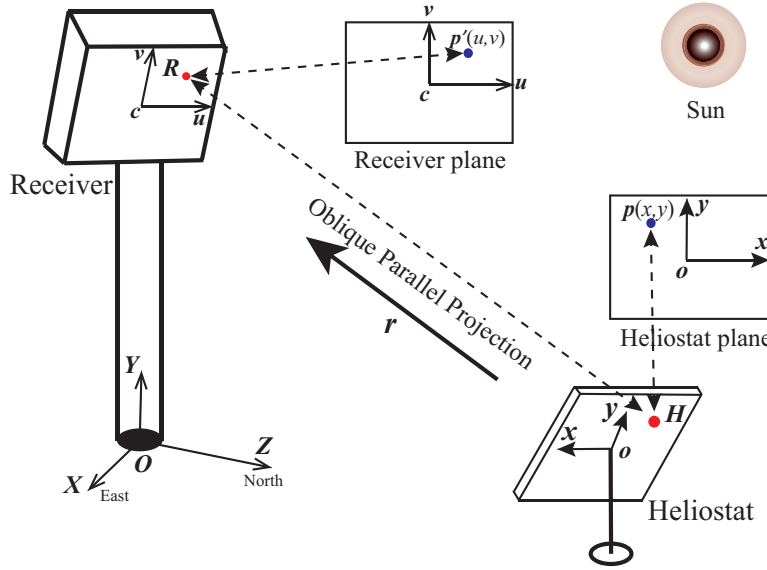

Figure 2: Three coordinate systems (namely, the global coordinate system $O\text{-}XYZ$ for the heliostat field, heliostat local coordinate system $o\text{-}xy$ for the heliostat plane and $c\text{-}uv$ for the receiver plane) and their relationships under oblique parallel projection.

3.2. Weiler-Atherton clipping algorithm

The proposed analytical flux density distribution model aims to handle shadowing and blocking effects accurately. Hence, the boundary of shadowed and blocked areas should be extracted. The task can be accomplished by the Weiler-Atherton clipping algorithm (Weiler and Atherton, 1977), which is designed for 2D Boolean operations (Boolean Operations on Polygons) and hidden surface removal in 3D computer graphics. Its inputs are two polygons and a Boolean operation between them, e.g., AND, OR, and NOT. It then returns the contours of the resultant polygon. The C open-source library and COM component implemented on a CPU for a 2D polygon Boolean operation are published online (Weiler Clip Library).The clipping algorithm has also

been adopted by Ramos and Ramos (2014); Cádiz et al. (2015); Kim et al. (2017). The proposed approach is same with those of Ramos and Ramos (2014); Kim et al. (2017). Cádiz et al. (2015) handled the shadowing and blocking problems by firstly projecting the underling heliostat and its shadowing and blocking heliostats to a common virtual plane, and then performing 2D polygon Boolean operations on the virtual plane. Its result is identical to the proposed method.

3.3. Quasi-Cauchy function

In the proposed model, a quasi-Cauchy function is adopted to analytically describe the smooth diffusion of the flux density distribution. This function was first introduced by McCormack and Sherstyuk (1998) as

$$h(r) = \frac{1}{(1 + s^2 r^2)^2}. \tag{2}$$

where r is the Euclidean distance and $s(s > 0)$ specifies the diffusion radius of the kernel, similar to the standard deviation parameter σ in the Gaussian function. The quasi-Cauchy function has been widely used for convolution surface modeling for multiple geometries, including points, lines, and arcs.

3.4. Green's theorem

The Green's theorem will be applied to obtain the closed-form solution to the analytical flux density distribution model, which is deduced in terms of a 2D convolution between a 2D polygon and a quasi-Cauchy function. This theorem (Buck, 2003) converts a double integral over a plane region $\mathcal{D}$ bounded by a positively oriented, simple closed curve $\mathcal{C}$ to the line integral along $\mathcal{C}$. Let Q and P be the functions of (x, y), which have continuous partial derivatives on an open region containing $\mathcal{D}$. Green's theorem states that

$$\iint_{\mathcal{D}} (\frac{\partial Q}{\partial x} - \frac{\partial P}{\partial y}) \mathrm{d}x \mathrm{d}y = \oint_{\mathcal{C}} (P \mathrm{d}x + Q \mathrm{d}y). \tag{3}$$

Specifically, if $P = 0$, we have

$$\iint_{\mathcal{D}} \frac{\partial Q}{\partial x} \mathrm{d}x \mathrm{d}y = \oint_{\mathcal{C}} Q \mathrm{d}y. \tag{4}$$

4. Numerical simulation with the ray tracing method

To derive and validate the proposed analytical model for the flux density prediction on the receiver, a state-of-the-art ray tracing method (Belhomme et al., 2009) is improved and implemented fully on a GPU with CUDA (Duan et al., 2019). The flowchart and schematic of the improved ray tracing algorithm are shown in Figure 3.

4.1. Ray tracing method for the flux density distribution simulation

First, each heliostat is assumed to be precisely adjusted through rotations about two axes so that the central ray from the sun is reflected from the heliostat center to the aiming point on the receiver.

The bidirectional ray tracing method (Belhomme et al., 2009) was adopted for the flux density distribution simulation, in which rays are generated directly on the underlying heliostat surface and traced along two directions: the incident direction and the reflection direction. In the method, the heliostat surface is uniformly tessellated into small pieces, called a micro-heliostat. At each micro-surface center, a bundle of rays (e.g., N_c rays) is generated. The directions of the rays are independently determined from the solar disc using an importance sampling approach (McCool and Fiume, 1992), i.e., more rays are generated from the center than
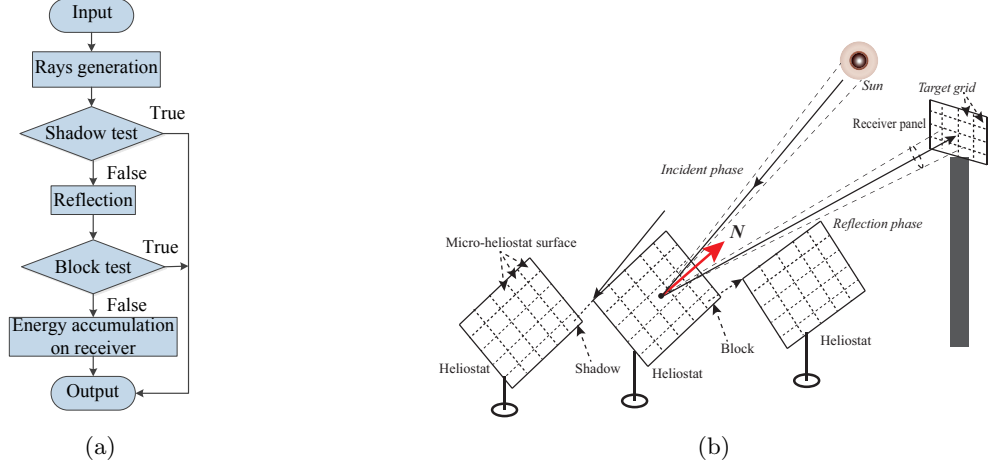
Figure 3: Flux density distribution simulation process based on ray tracing: (a) flow chart of the ray tracing method; (b) the incident rays are generated from the sun cone, which are defined according to the sun shape model(Buie et al., 2003). They are then reflected according to the micro-surface's normal, which is determined by the slope error. Shadowing and blocking effects are determined discretely by intersection detection of the incident and reflected rays, respectively.

from the rim of the sun according to the sun shape model (Buie et al., 2003). The CSR of the sun shape model is assumed to be 0.2 (Belhomme et al., 2009). In the incident phase, each ray is checked to determine whether it collides with other heliostats (shadow test). The ray collision detection is accomplished by a ray traveling algorithm, i.e., the 3D-DDA algorithm proposed by Fujimoto et al. (1986) and implemented on a GPU, which can exploit the spatial coherence efficiently. If a ray collides with a heliostat, the ray tracing process terminates. Otherwise, the incident rays are reflected according to the local micro-heliostat's normal, which is modeled as an isotropic Gaussian distribution (with standard deviation σ_s, i.e., slope error) of the angular deviation from the ideal position (Landman et al., 2016). A rough heliostat surface corresponds to a larger σ_s, and vice versa. Next, the reflected rays are traced along the reflection direction with the 3D-DDA algorithm for the block test. The tracing process for a ray will terminate if the ray collides with a heliostat on the way to the receiver.

The receiver plane is also tessellated into grids uniformly. If a ray reaches the receiver, its associated energy (W) is accumulated in the corresponding target grid on the GPU. The energy of each incident ray on the same micro-heliostat surface is equally determined as follows:

$$E_{ray} = \frac{I_D * S_{sub} * \cos \omega * \rho}{N_c} * \eta_{aa} \ (\text{W}), \tag{5}$$

where I_D is the solar DNI in W/m^2, S_{sub} represents the area of one micro-heliostat surface, ω is the angle between the sunlight direction and micro-surface normal, ρ is the heliostat surface reflectivity and N_c is the number of incident rays sampled on a micro-heliostat surface. η_{aa} is the atmospheric attenuation factor, which is related to the slant length d between the heliostat and the receiver (Leary et al., 1979):

$$\eta_{aa} = \begin{cases} 0.99321 - 0.0001176 * d + 1.97 * 10^{-8} * d^2 & d \leq 1000 \text{ m} \\ e^{-0.0001106*d} & d > 1000 \text{ m} \end{cases} \tag{6}$$

4.2. Validation of the ray tracing simulation against real data

To verify the accuracy of the proposed ray tracing method, a validation step is conducted by comparing the simulation results with the measured data and the results from Soltrace (Wendelin, 2003; Soltrace project) and Tonatiuh (Blanco et al., 2005; Tonatiuh project) software. The parameters of the two experimental heliostatsare

7

Table 1: Basic field parameters in the ray tracing validation

sun parameters			heliostat (1.6 m × 1.25 m) (ρ=0.88, σ_s=2.0 mrad)		receiver panel (4.6 m × 4.6 m)	
azimuth	elevation	DNI (W/m^2)	heliostat id	position	center	normal
-168.06°	53.83°	800.0	S_R108	(90.97, 3.91, -20.97)	(0.0, 55.0, 0.0)	(0.71, 0.0, -0.71)
-173.09°	41.52°	750.0	N_R028	(84.05, 6.29, 35.13)	(0.0, 55.0, 0.0)	(0.71, 0.0, 0.71)

given in Table 1. The geometry of the heliostat was measured discretely, as shown in Figure 4. These heliostats were adjusted to reflect the sunlight to the center of the target panel at two specific times with the azimuth-elevation tracking model (Chen et al., 2004). The photographic images of the flux spots on the receiver panel were captured by an industrial camera (Figure 5a). Then, the target area pre-marked by four labels on the panel was clipped and rectified as a rectangular region according to the camera parameters (Figure 5b). To eliminate the ambient flux component, the average pixel value of four sampled regions along the image edges were calculated and subtracted from the whole image. The resultant flux spot (Figure 5c) represents the net solar energy reflected by the heliostat.
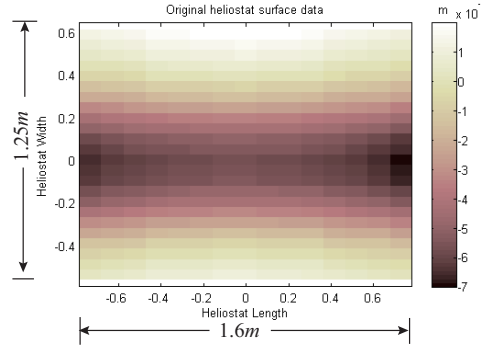

Figure 4: Measured geometry of the experimental heliostat: the range of the color bar is from -7.0 × 10^{-4} m to 1.0 × 10^{-4} m, representing the depth (negative) or elevation (positive) of each square with respect to an imaginary flat plane over the heliostat.

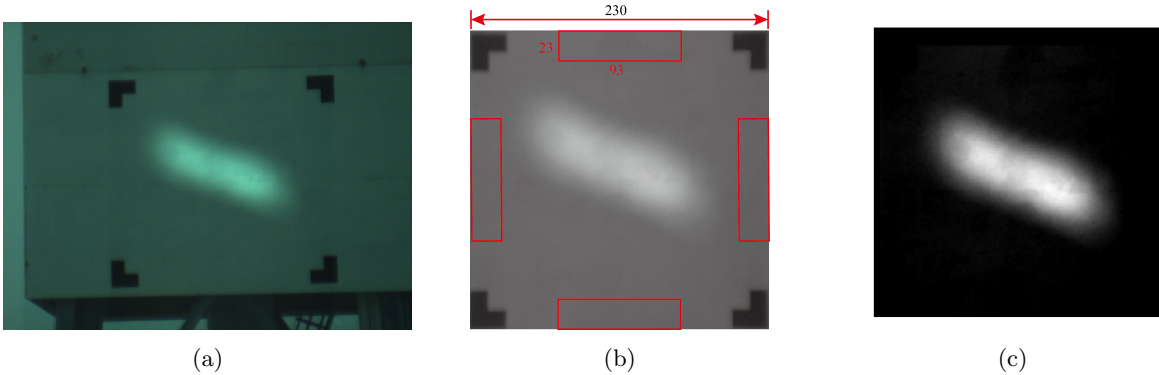

(a)   (b)   (c)

Figure 5: Preprocessing of the real flux spot image for ray tracing validation: (a) image capture of the flux spot on the receiver; (b) image correction and ambient flux component extraction; (c) net solar flux reflected by the heliostat.

All the parameters of the experimental heliostats were exactly set and passed to our GPU-based ray tracing

simulation engine. The tessellation granularities for the heliostat and receiver plane were 1 cm and 2 cm, respectively. On each micro-heliostat surface, 2048 rays were generated. Consequently, 40,960,000 rays were traced on each heliostat. The simulation results based on the measured heliostat geometry or flat heliostat assumption (just as Soltrace and Tonatiuh do) are presented in Figure 6, along with the measured ground truth results and the results of Soltrace and Tonatiuh. As it shows, the flux density distribution results from the proposed improved ray tracing method are well consistent with the real measured data. In Soltrace and Tonatiuh, same number of rays are traced for each heliostat. Since the ray tracer engines cannot take the heliostat surface with measured geometry as input in Soltrace and Tonatiuh, the heliostat surface is treated as a flat plane. As a result, the flux spots predicted by Soltrace and Tonatiuh appear more diffuse than the ground truth, which are consistent with that by the proposed ray tracing method under flat heliostat assumption. The runtimes of our ray tracing, Soltrace and Tonatiuh are 11.22 ms (GPU), 5250 ms (multithreading on CPU) and 10120 ms (multithreading on CPU), respectively.
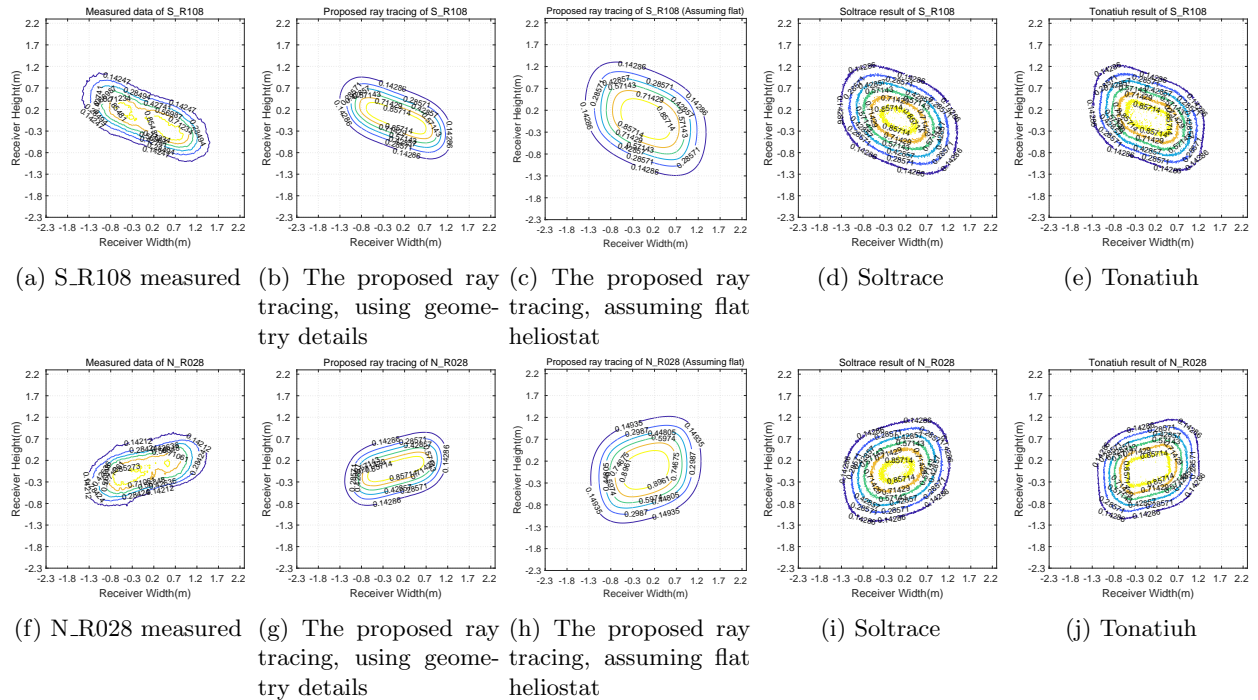

Figure 6: Comparison of the measured flux spot (1st column) with the flux contours of the proposed improved ray tracing method using the heliostat detail geometry (2rd column), proposed ray tracing assuming flat heliostats (3rd column), the Soltrace results (4th column) and the Tonatiuh results (5th column).

From the above experiments and comparisons, it can be concluded that the proposed ray tracing simulation engine is reliable, accurate and versatile and is therefore competent for the subsequent analytical flux density model derivation.

5. Theoretical analysis of the flux density distribution model

In this section, we analyze the flux density modeling process from a theoretical point of view and introduce the concept of the imaginary flux density scalar field (IFDSF) defined in the heliostat local coordinate system.

A flat heliostat projects a flux spot on the receiver plane, which is roughly the principal image of the heliostat with overlays of the solar disc (Elsayed et al., 1995; Lovegrove and Stein, 2012). This spot is enlarged

due to the imperfect reflection of the mirror. Consequently, the flux density distribution on the receiver is determined in practice by the sunlight direction and sun shape, the heliostat position, size, orientation and mirror slope errors (Elsayed et al., 1995), as shown in Figure 7.
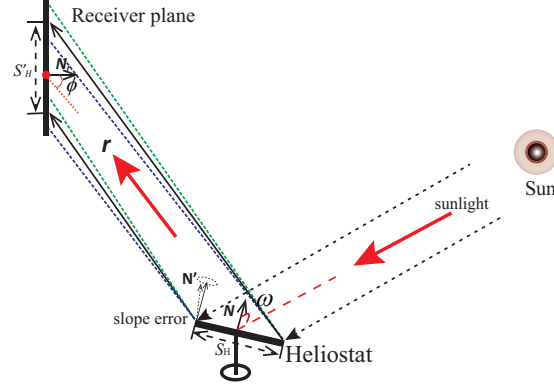

Figure 7: The flux density distribution on the receiver plane is influenced by the sun shape, the heliostat position, orientation, size and micro-heliostat surface slope error, among other factors.

Since the flux spot on the receiver is reflected by the heliostat mirror, it is reasonable to first derive an IFDSF in the 2D heliostat coordinate system and then project this scalar field function to the receiver surface along the reflection direction. The flux density value (the atmospheric effect is included) of a point on the receiver equals to the value of the corresponding point on the heliostat under parallel projection. García et al. (2015) noted that this procedure can describe the distorted flux spot on the receiver more reasonably.

According to the geometric relationship between the receiver surface and the heliostat in Figure 7, we have

$$S_H \cdot \cos \omega = S'_H \cdot \cos \phi, \tag{7}$$

where S_H is the heliostat surface area, ω is the angle between the sunlight direction and the heliostat surface normal, and S'_H is the projection area of the corresponding heliostat surface on the receiver plane under parallel projection along the reflection direction. ϕ is the angle between the heliostat reflection direction and the receiver plane normal.

The principle of energy conservation states that the energy reaching the receiver surface is equal to that reflected by the heliostat, minus the relevant losses. Thus, the uniform flux density on the receiver surface under the assumptions of ideal mirror reflection and directional light of the sun is

$$A = \frac{P_h \cdot \eta_{aa}}{S'_H} = \frac{I_D \cdot S_H \cdot \cos \omega \cdot \rho \cdot \eta_{aa}}{S'_H} = I_D \cdot \rho \cdot \eta_{aa} \cdot \cos \phi \ (\text{W/m}^2), \tag{8}$$

where P_h is the total energy reflected by the heliostat, which equals to a product of the solar DNI (I_D), the heliostat surface area (S_H), the heliostat cosine effect ($\cos \omega$) and the heliostat reflectivity (ρ). η_{aa} is the atmospheric attenuation factor.

For an ideal flat heliostat, the IFDSF should be constant, as depicted by the green box in Figure 8a. However, due to the influences of the sun shape and heliostat micro-surface slope error in practice, the reflected flux beam is scattered, which is usually characterized by the "diffusion radius" of the flux spot on the receiver surface. The actual IFDSF contains a smooth transition around the heliostat edges, as shown in Figure 8c. Intuitively, the field can be mathematically described as a convolution between the uniform IFDSF and a proper convolution kernel. Further, to make the convolution integrable, the quasi-Cauchy function (2) is adopted as the convolution kernel to model the flux density diffusion effects on the receiver surface analytically.
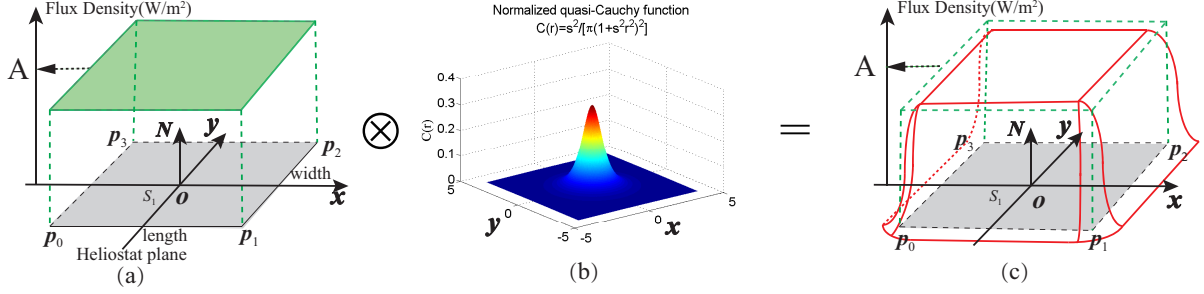
Figure 8: The IFDSF on the heliostat surface (c) can be depicted as a smoothly diffused function, sketched by the red line, as derived from the convolution of the uniform IFDSF (a) and a normalized quasi-Cauchy kernel function (b).

6. Modeling the flux density distribution with a closed-form expression

Based on the analysis in Section 5, the proposed modeling process for the flux density distribution on the receiver consists of three steps. First, the effective heliostat reflection surface area is extracted, which takes shadowing and blocking effects into account. Second, an analytical model with a closed-form expression for the imaginary flux density distribution defined in the heliostat coordinate system is derived. Finally, the imaginary distribution is projected to the receiver surface along the reflection direction through an oblique parallel projection.

6.1. Effective heliostat reflection surface area extraction

First, the shadowing and blocking effects among the heliostats in the field are determined in parallel on the GPU with the light beam traversal algorithm (He et al., 2017). Then, the shadowing or blocking heliostats are projected on the underlying heliostat, and the shadowed and blocked areas are precisely clipped by employing the Weiler-Atherton algorithm. As a result, a heliostat whose shadowed or blocked areas are trimmed out is obtained, which is also called the effective heliostat reflection surface area (Figure 9).

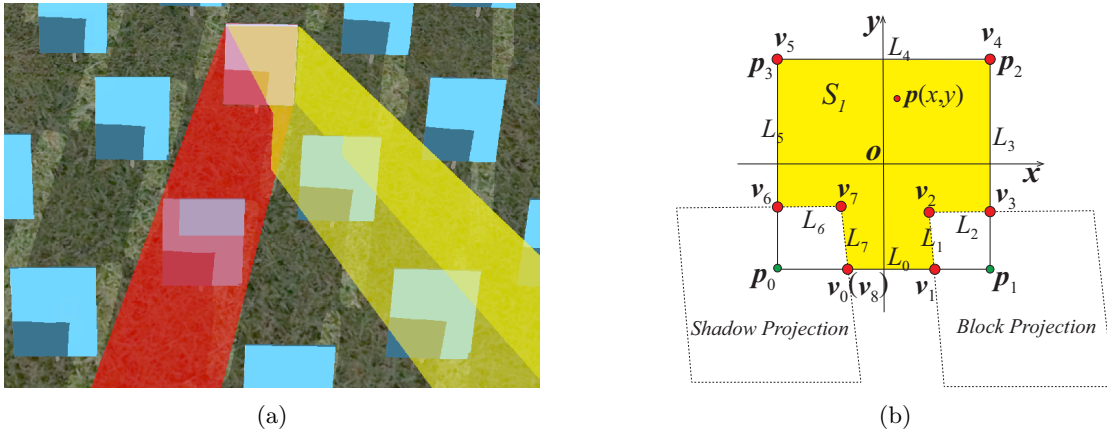Figure 9: (a) The incident solar beam (red parallelepiped) and reflected beam (yellow parallelepiped) of a heliostat, which are occluded by the neighbor heliostats, causing shadowing and blocking effects in the heliostat field; (b) the effective reflection surface (yellow area S_1) of the heliostat defined in the 2D heliostat local coordinate system along with the shadowing and blocking areas caused by the neighbor heliostats.

6.2. Modeling of an IFDSF on the heliostat

In this section, we derive a closed-form expression of the imaginary flux density scalar field $F(x, y)$ defined in the heliostat local coordinate system, which represents the flux density of the projected points on the receiver surface along the reflection direction of the heliostat.

In the 2D heliostat local coordinate system $\boldsymbol{o\text{-}xy}$, as shown in Figure 9b, the effective reflecting surface area of the heliostat S_1 is a planar polygon in general, whose vertices are $\{\boldsymbol{v}_i\}_{i=0}^{n-1}$ and edges are $\{L_i\}_{i=0}^{n-1}$. Each edge L_i from $\boldsymbol{v}_i(x_i, y_i)$ to $\boldsymbol{v}_{i+1}(x_{i+1}, y_{i+1})$ can be parameterized as follows:

$$L_i(t) : \begin{cases} \tilde{x}_i(t) = x_i + a_i t \\ \tilde{y}_i(t) = y_i + b_i t \end{cases}, t \in [0, 1], \tag{9}$$

where

$$a_i = x_{i+1} - x_i, b_i = y_{i+1} - y_i, \boldsymbol{v}_n(x_n, y_n) = \boldsymbol{v}_0(x_0, y_0).$$

Based on the analysis in Section 5, for any point $\boldsymbol{p}(x, y)$ on the 2D heliostat plane, as shown in Figure 9, the imaginary flux density of $\boldsymbol{p}$ can be modeled as the convolution between the uniform IFDSF $H(\boldsymbol{q})$ (as shown in Figure 8) and a normalized quasi-Cauchy function $C(k)$ over the heliostat plane. Let $\tilde{F}(\boldsymbol{p})$ be

$$\tilde{F}(\boldsymbol{p}) = \tilde{F}(x, y) = (H \otimes C)(\boldsymbol{p}) = \iint H(\boldsymbol{q})C(||\boldsymbol{p} - \boldsymbol{q}||)\mathrm{d}\boldsymbol{q}, \tag{10}$$

where

$$H(\boldsymbol{q}) = \begin{cases} A, & \boldsymbol{q} \in S_1 \\ 0, & \text{else} \end{cases}, \quad C(k) = \frac{s^2}{\pi} \frac{1}{(1 + s^2 k^2)^2}, \tag{11}$$

and A is defined in (8).

Therefore,

$$\tilde{F}(x, y) = \iint_{S_1} A \cdot \frac{s^2}{\pi} \frac{1}{(1 + s^2((x - \tilde{x})^2 + (y - \tilde{y})^2))^2} \mathrm{d}\tilde{x}\mathrm{d}\tilde{y}. \tag{12}$$

Considering Green's Theorem (4), we set

$$\frac{\partial Q(\tilde{x}, \tilde{y})}{\partial \tilde{x}} = \frac{1}{(s^{-2} + (x - \tilde{x})^2 + (y - \tilde{y})^2)^2}, \tag{13}$$

then

$$\begin{aligned} Q(\tilde{x}, \tilde{y}) &= \int \frac{\partial Q(\tilde{x}, \tilde{y})}{\partial \tilde{x}} \mathrm{d}\tilde{x} \\ &= \frac{1}{2} \Big(\frac{\tilde{x} - x}{(s^{-2} + (\tilde{y} - y)^2)(s^{-2} + (\tilde{x} - x)^2 + (\tilde{y} - y)^2)} \\ &\quad + \frac{\arctan \frac{\tilde{x} - x}{\sqrt{s^{-2} + (\tilde{y} - y)^2}}}{(s^{-2} + (\tilde{y} - y)^2)^{\frac{3}{2}}} \Big). \end{aligned} \tag{14}$$

Combining (4), (9), (12) and (13), we have

$$\begin{aligned} \tilde{F}(x, y) &= A \cdot \frac{s^2}{\pi} \cdot \frac{1}{s^4} \iint_{S_1} \frac{\partial Q(\tilde{x}, \tilde{y})}{\partial \tilde{x}} \mathrm{d}\tilde{x}\mathrm{d}\tilde{y} \\ &= A \cdot \frac{1}{\pi \cdot s^2} \oint_{\mathcal{C}} Q(\tilde{x}, \tilde{y})\mathrm{d}\tilde{y} = A \cdot \frac{1}{\pi \cdot s^2} \sum_{i=0}^{n-1} \int_0^1 Q(\tilde{x}, \tilde{y}) \cdot b_i \mathrm{d}t, \end{aligned} \tag{15}$$

$\mathcal{C}$ is the boundary of region S_1, i.e., the union of $\{L_i\}_{i=0}^{n-1}$. Let I_i and $f_i(t)$ be

$$f_i(t) = \int Q(\tilde{x}, \tilde{y}) \cdot b_i \mathrm{d}t, \quad I_i = \int_0^1 Q(\tilde{x}, \tilde{y}) \cdot b_i \mathrm{d}t = f_i(1) - f_i(0). \tag{16}$$

Substituting (9) and (14), $f_i(t)$ is solved as follows:

$$f_i(t) = \frac{1}{4} b_i \Big(\frac{2S_4 \sqrt{S_1} \arctan(S_5/\sqrt{S_1})}{b_i m S_2} + 2b_i S_3 \frac{\arctan(S_5/\sqrt{S_1})}{\sqrt{S_1} S_2}$$
$$+ \frac{2S_7 \arctan(\frac{S_6}{\sqrt{m+S_7^2}})}{b_i m \sqrt{m + S_7^2}} + a_i \frac{\log(S_8)}{S_2} - a_i \frac{\log(b_i{}^2 S_8)}{S_2} \Big), \tag{17}$$

in which

$$\begin{cases} m = 1/s^2, \\ S_1 = b_i^2 (m + (x - x_i)^2) + a_i^2 (m + (y - y_i)^2) - 2a_i b_i (x - x_i)(y - y_i), \\ S_2 = b_i^2 (x - x_i)^2 + a_i^2 (m + (y - y_i)^2) - 2a_i b_i (x - x_i)(y - y_i), \\ S_3 = b_i (x - x_i) + a_i (-y + y_i), \\ S_4 = b_i (-x + x_i) + a_i (y - y_i), \\ S_5 = a_i^2 t + a_i (-x + x_i) + b_i (b_i t - y + y_i), \\ S_6 = a_i t - (x - x_i), \\ S_7 = b_i t - (y - y_i), \\ S_8 = m + S_6{}^2 + S_7{}^2 \end{cases} \tag{18}$$

$f_i(0)$ and $f_i(1)$ can be easily expressed as in Appendix A. From (15), we obtain

$$\tilde{F}(x,y) = A \cdot \frac{1}{\pi \cdot s^2} \sum_{i=0}^{n-1} I_i = A \cdot \frac{1}{\pi \cdot s^2} \sum_{i=0}^{n-1} (f_i(1) - f_i(0)). \tag{19}$$

The normalized quasi-Cauchy kernel function $C(r)$ (11) is defined over the whole 2D plane, while the receiver surface area is limited. Considering energy conservation, the flux density expression (19) should be normalized by dividing by the kernel function's integral (C_g) over the receiver panel's projection (S_{recv_proj}) on the heliostat plane. Finally, the imaginary flux density of point $\boldsymbol{p}(x, y)$ is defined as follows:

$$F(x, y) = \tilde{F}(x, y)/C_g, \tag{20}$$

where

$$C_g = \frac{s^2}{\pi} \iint_{S_{recv\_proj}} \frac{1}{(1 + s^2(\tilde{x}^2 + \tilde{y}^2))^2} \mathrm{d}\tilde{x} \mathrm{d}\tilde{y}. \tag{21}$$

C_g is similar to $\tilde{F}(x, y)$ in (12) and can be analytically computed along the silhouette of S_{recv_proj} in an analogous way. We omit the derivation here due to length limitations.

An example of an IFDSF on the heliostat surface in Figure 9b is shown in Figure 10, calculated analytically with (20), where the heliostat is 2 m × 2 m, A = 600 W/m^2 and $s = 3.2$.
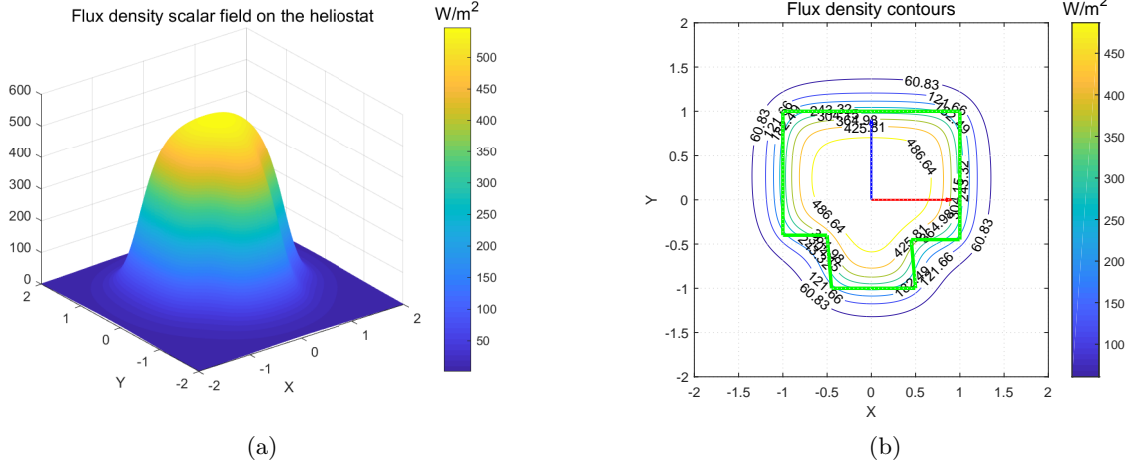
Figure 10: Example of an IFDSF (a) and flux density contours (b) corresponding to the effective heliostat reflection area in Figure 9b, calculated analytically by (20).

6.3. Oblique parallel projection

The resultant flux density distribution on the receiver surface can be obtained by directly mapping the imaginary flux density scalar field on the heliostat to the receiver through an oblique parallel projection, as shown in Figure 2.

In the global coordinate system $\boldsymbol{O\text{-}XYZ}$, let $\boldsymbol{R} = (R_x, R_y, R_z)$ be a point on the receiver surface, and let $\boldsymbol{H} = (H_x, H_y, H_z)$ be the corresponding point on the heliostat under an oblique parallel projection (Figure 2); then,

$$\boldsymbol{H} = (\mathbf{I} - \frac{1}{\boldsymbol{N} \cdot \boldsymbol{r}} \boldsymbol{r}^{\mathrm{T}} \boldsymbol{N}) \boldsymbol{R} + \frac{\boldsymbol{N} \cdot \boldsymbol{o}}{\boldsymbol{N} \cdot \boldsymbol{r}} \boldsymbol{r}, \tag{22}$$

where $\boldsymbol{r} = (r_x, r_y, r_z)$ is the reflection direction of the underlying heliostat. $\boldsymbol{N} = (N_x, N_y, N_z)$ is the heliostat surface normal, and $\boldsymbol{o} = (o_x, o_y, o_z)$ is the heliostat center. $\mathbf{I}$ is the unitary matrix. For the detailed derivation of (22), refer to Appendix B

6.4. The model parameter "s"

In general, the ray tracing method is regarded as an accurate method for flux density distribution simulation. The simulation result obtained via ray tracing can be used as the ground truth. To determine the parameter "s" in the Cauchy kernel function (11), it is necessary to make the difference between the analytical flux density distribution and the ground truth as small as possible. One of the difference measurements is the root mean squared error (e_{rms}):

$$e_{rms} = \sqrt{\frac{\sum_{i=1}^{N}(F_i{}^a - F_i{}^r)^2}{N}} \ (\mathrm{W/m^2}), \tag{23}$$

where N is the number of the grids on the receiver surface and $F_i{}^a$ and $F_i{}^r$ stand for the flux density values of the proposed analytical method and the ground truth value obtained via the ray tracing method at the ith grid, respectively.

In addition to the e_{rms}, which describes the difference globally, the flux peak difference is also important since the flux peak results in the highest temperature on the receiver. To this end, a weighted objective function

14

is defined for optimizing the parameter "s" in the proposed model:

$$\arg\min_{s}\{\alpha * e_{rms} + (1 - \alpha) * ||F_{max}{}^{a}(s) - F_{max}{}^{r}||\},\qquad(24)$$

where $F_{max}{}^{a}$ and $F_{max}{}^{r}$ represent the flux peaks of the proposed analytical method and the ground truth, respectively. α is a tunable parameter for practical applications, e.g., the global optimum ($\alpha = 1$) or peak optimum ($\alpha = 0$). We set $\alpha = 0.5$ in this paper. In the work by Collado (2010), the parameter σ in the HFLCAL model is obtained by minimizing the peak difference, referred as one-point fitting, which is a special case of our optimization. We also propose two error metrics to quantitatively evaluate the analytical models: the flux power error (e_{power}) and peak error (e_{peak}). These metrics are defined as follows:

$$e_{power} = \frac{||P^{a} - P^{r}||}{P^{r}}\ (\%),\quad e_{peak} = \frac{||F_{max}{}^{a} - F_{max}{}^{r}||}{F_{max}{}^{r}}\ (\%),\qquad(25)$$

where P^{r} and P^{a} are the flux power predicted by the ray tracing method and the analytical model, and F_{max}^{r} and F_{max}^{a} represent the flux peak of the ray tracing method and the analytical model, respectively.

In theory, the parameter "s" in the Cauchy kernel function (11) controls the diffusion effect of the reflected flux spot on the receiver. The diffusion effect is complex and related to many factors, such as the sun position, the sun shape, the distance between the heliostat and receiver, the heliostat position, the heliostat mirror slope error, the atmospheric attenuation and scattering, etc. Among these factors, it can be assumed that sunshape, heliostat mirror slope error, atmospheric attenuation and scattering are fixed to some extent for a specific heliostat in a given heliostat field. Thus the sun position and the heliostat position are two main factors for diffusion effect. Similar to the HFLCAL model, where the diffusion effect is simply controlled by a parameter "σ", the diffusion effect in the proposed model is also controlled by a parameter "s" in a simplified way. According to our experiments, the range of "s" is 0.3~2.5. When the sun position is changed, the variation of the parameter "s" is very small, e.g. $-0.1 \sim 0.1$. As a result, the parameter "s" is mainly related with the heliostat position. Therefore, a practical method to estimate the parameter "s" for each heliostat would be: first, calculating the "s" values by optimizing the proposed model against the ground truth (Collado, 2010) at several sampled times (different sun positions), e.g. 12 in a day; second, averaging the estimated "s" values and setting the mean value as the "s" for the heliostat.

7. Experiments and comparisons

In this section, we demonstrate the accuracy and efficiency of the proposed analytical model through experiments and comparisons.

The proposed analytical flux density distribution model was implemented in a versatile GPU rendering-pipeline-based framework (He et al., 2017) on a desktop PC with an Inter core (TM) i5-3450 @3.10 GHz CPU and an NVIDIA GeForce GTX 1080 GPU.

Table 2: Two sun conditions for the experiment and comparison

	Altitude	Azimuth	DNI(W/m^2)
Midday	83.15°	88.0°	1000.0
Late afternoon	10.0°	162.0°	600.0

A synthesized radially staggered heliostat field is designed for the experiments, based on the algorithm proposed by Lipps and Vant-Hull (1978), as shown in Figure 11. Two representative sun positions (Table 2)

Table 3: Parameters of the heliostats used in the experiment and comparison

Heliostat id	x(m)	y(m)	z(m)	Radius (m)	Azimuth (rad)
137	67.82	2.0	72.77	99.47	0.75
1042	61.43	2.0	192.32	201.89	0.31
1060	165.84	2.0	115.14	201.89	0.96
2255	-71.64	2.0	297.54	306.04	-0.23
2307	256.27	2.0	167.31	306.04	0.99
3595	-10.96	2.0	408.52	408.66	-0.03
6067	-304.53	2.0	517.74	600.66	-0.53
7575	513.43	2.0	492.76	711.64	0.81
8677	70.94	2.0	805.09	808.21	0.08
9716	17.43	2.0	898.67	898.87	0.01

are chosen. One is in the middle of the day, and the other is in the late afternoon when the sun is low and thus the shadowing and blocking effects are obvious. The size of the heliostat is 3.2 m× 2.2 m, and its reflectivity is 0.88. The standard deviation of the heliostat slope error is assumed to be 2.0 mrad. Ten heliostats were sampled, whose distances to the receiver ranged from approximately 100.0 m to 900.0 m. The parameters of the selected heliostats are listed in Table 3. All the heliostats are aiming at the center (0.0, 137.0, 1.0) of the receiver plane, which is 12 m × 12 m and its normal $\boldsymbol{N}_r = (0.0, 0.0, 1.0)$. The resolutions of the receiver surface tessellation in the ray tracing method and the proposed analytical method are identically set as 5×5 cm^2 to accommodate the trade-off between simulation accuracy and efficiency.
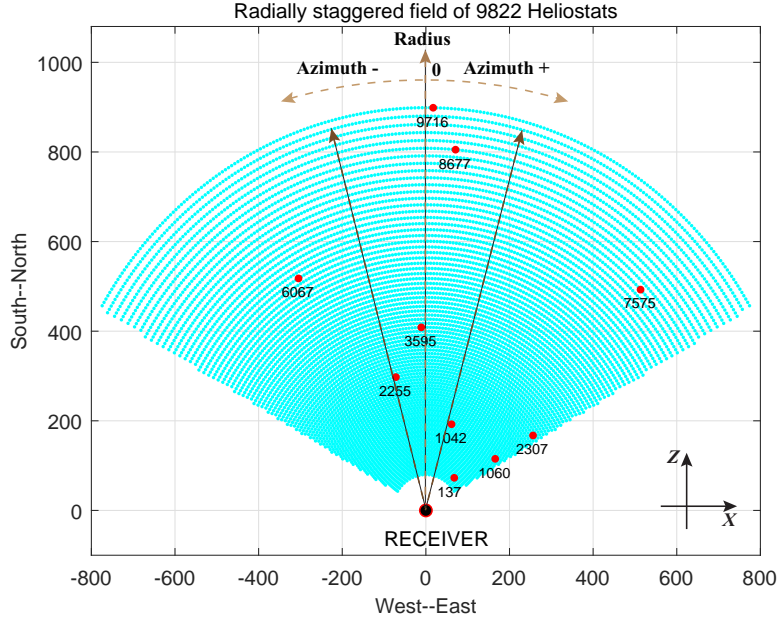

Figure 11: A radially staggered heliostat field is created. The heliostats being investigated are indicated with their indexes.

In the ray tracing simulation, the heliostat surface is tessellated into $320 \times 220 = 70400$ micro-heliostat surfaces. At each micro-heliostat surface, 4096 rays are generated, i.e., a total of 288 million rays are traced. We compare the proposed model with the ray tracing method and the refined HFLCAL model (García et al., 2015) from the aspects of accuracy and runtime. The refined HFLCAL model was also implemented in the

same rendering-pipeline-based framework.

7.1. Flux density distribution results and comparisons

Figure 12 and Figure 13 show comparisons of the flux density distribution simulation results of selected heliostats among the ray tracing method, the proposed analytical model and the refined HFLCAL model (García et al., 2015). The corresponding statistics of the metrics (e_{power} and e_{peak} (25) and the e_{rms} (23)) are shown in Figure 14. Only some of the selected heliostats were presented due to the limited space.

Several conclusions can be drawn. First, the proposed model accurately predicts the gross flux power with and without shadowing and blocking effects, while the HFLCAL model manifests relative large error when shadowing or blocking effects exist. Second, both models can predict the peak value with a very small error of less than 0.3%. The HFLCAL model is slightly better since it is directly optimized with the peak deviation. Third, the e_{rms} of the proposed model is always less than that of the HFLCAL model for the heliostats close to the receiver and those with shadowing and blocking effects, indicating a more accurate description of the flux density distribution. Some e_{rms} is comparably small for the heliostats in the midday case.

The proposed model can naturally take the heliostat position, size, slope error, orientation and shadowing and blocking effects into account since it is based on a convolution on the effective reflection surface area, where shadowed or blocked areas are eliminated. On the other hand, the HFLCAL model depicts the flux spot with a simple Gaussian distribution without considering the heliostat size or shadowing or blocking effects. Consequently, the flux spots predicted by the proposed analytical method are more consistent with the ground truth than those predicted by the HFLCAL model, from the aspects of flux spot shapes and distributions. Further, in the proposed model, the flux density distribution near the boundary of the effective reflection surface exhibits a smooth transition from lightness to darkness, which is consistent with the ray tracing result and a previous report (Elsayed et al., 1995). In contrast, the results of the HFLCAL model exhibit a relatively large deviation of the flux density distribution, particularly in the blocked or shadowed area, and an overestimation of the gross power incident on the receiver (Figure 13, Figure 14d).

Note that the HFLCAL model was initially proposed to assist in heliostat field layout design and optimization (Schwarzbözl et al., 2009), which do not necessarily require accurate flux density prediction on the receiver. In fact, the HFLCAL model works well for some flat heliostats far from the receiver (Figure 12f, Figure 13f). For these heliostats, the effects of the sun shape and heliostat slope error are the dominant factors compared to the heliostat size. Besides, particular errors compensate each other for these cases. Meanwhile, the proposed model also adapts to these cases and achieves accurate results.

7.2. Computational efficiency

The implementation of the proposed model consists of two steps: effective reflection surface extraction on CPU and flux calculation on GPU. The corresponding average time costs of the two steps are 2.0 ms and 0.8 ms respectively. The proposed ray tracing engine is efficient. On average, it takes about 51 ms to trace 288 million rays for simulating a single heliostat. The data I/O cost of all the 9822 heliostats between GPU and CPU is 3∼5 milliseconds, which is almost negligible.

As a state-of-the-art analytical model with a closed-form expression, the HFLCAL model (García et al., 2015) depicts the flux spot on the receiver with an oblique Gaussian distribution, which is much simpler than our model. However, prediction accuracy is sacrificed to some extent, particularly when the heliostat is partially shadowed or blocked by other heliostats, as described in Section 7.1. In the GPU implementation of the HFLCAL model, the flux density calculation takes approximately 0.6 ms.
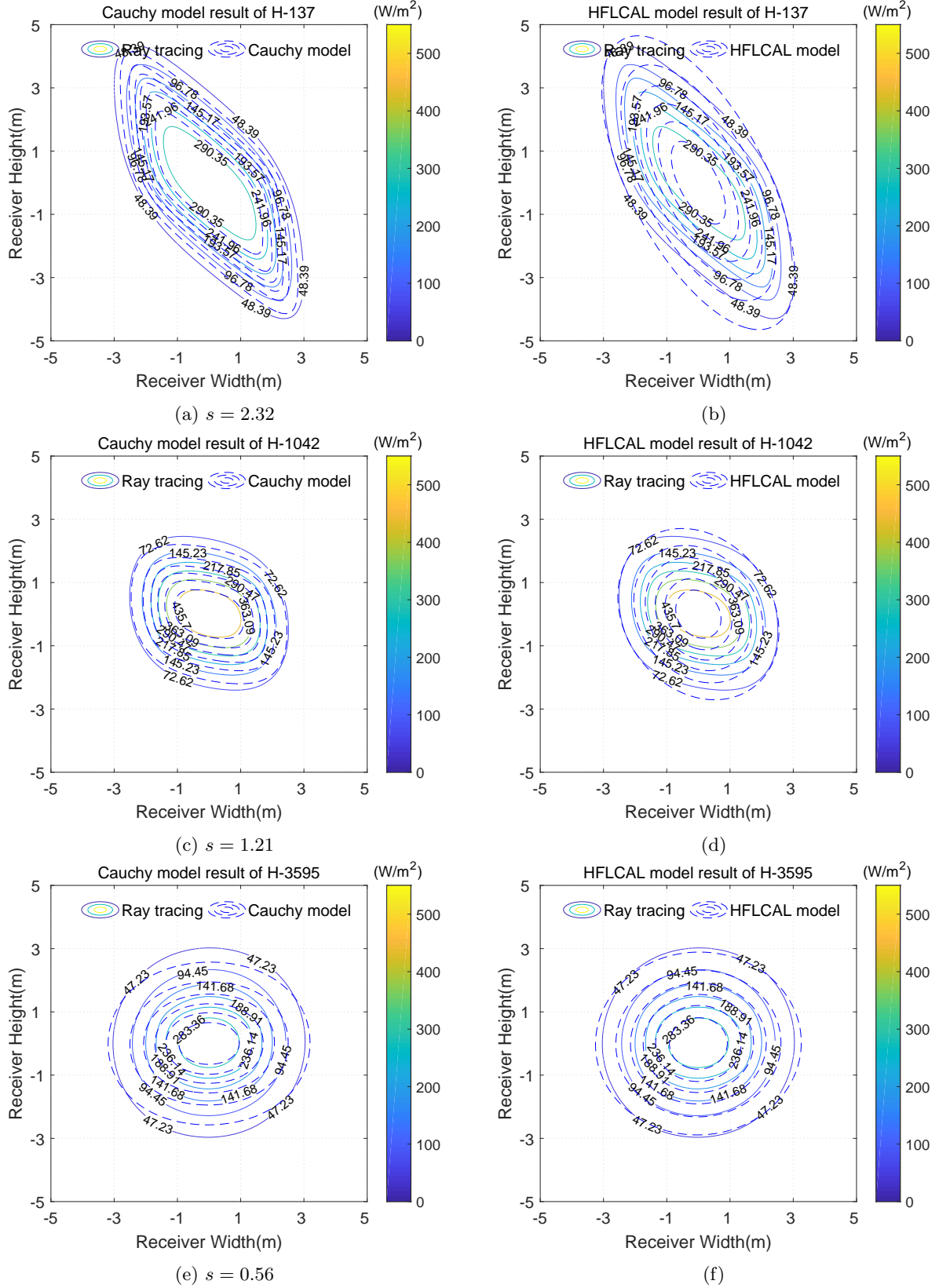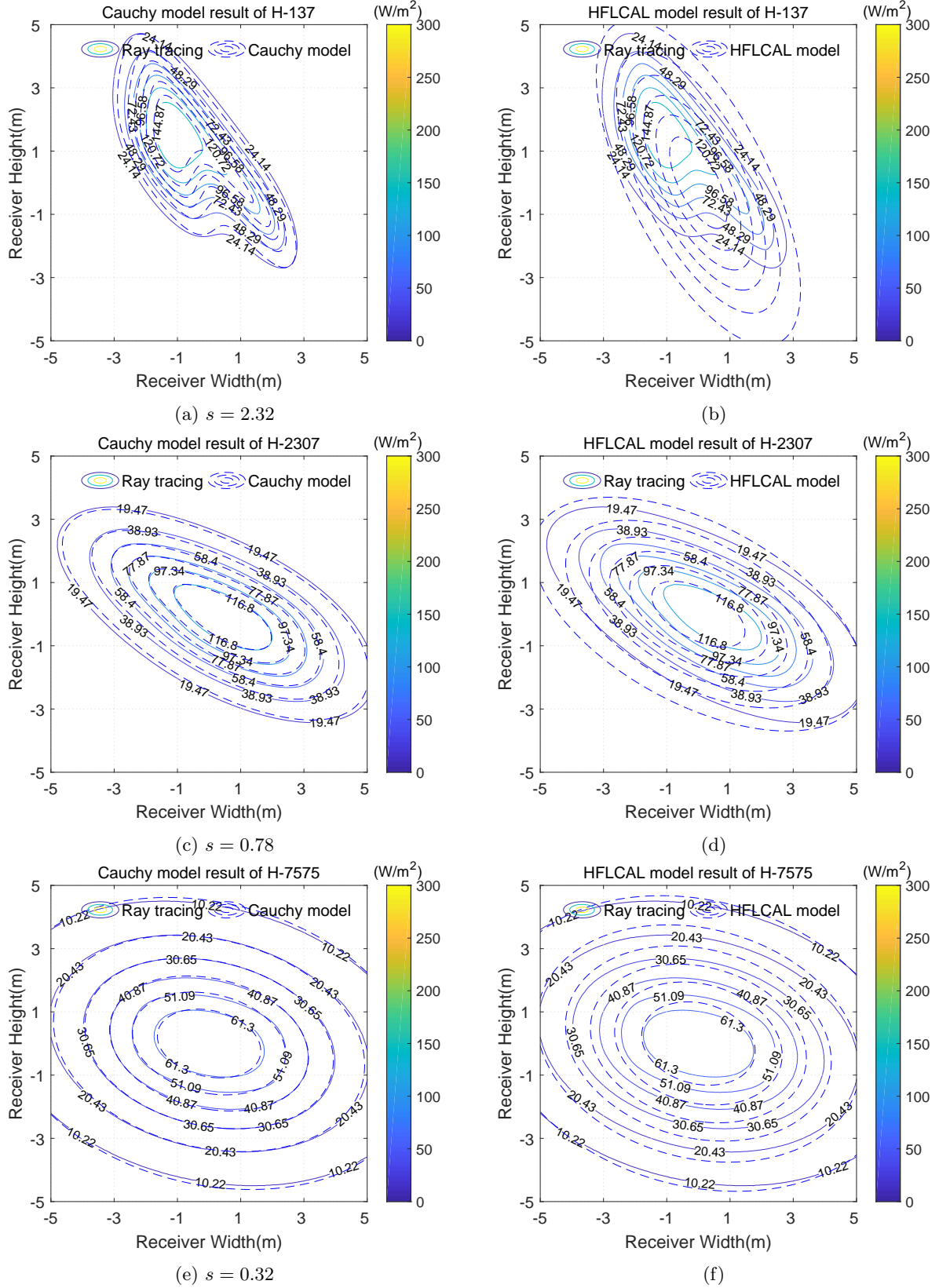
Figure 12: Comparison of the simulation results of the proposed analytical model (left column) and the refined HFLCAL model (right column) in the midday. The simulation results based on ray tracing (solid line) are regarded as the ground truth.

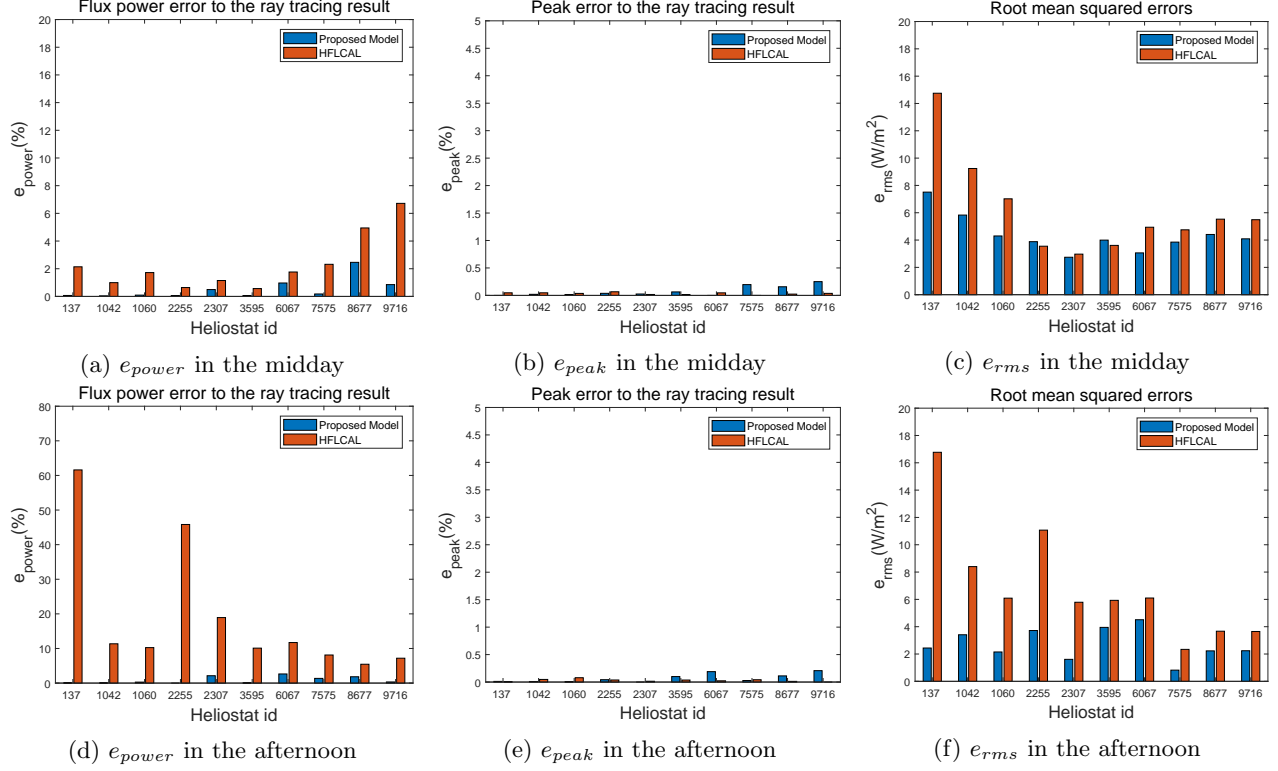Figure 13: Comparison of the simulation results of the proposed analytical model (left column) and the refined HFLCAL model (right column) in the afternoon. The simulation results based on ray tracing (solid line) are regarded as the ground truth.

(a) e_{power} in the midday   (b) e_{peak} in the midday   (c) e_{rms} in the midday

(d) e_{power} in the afternoon   (e) e_{peak} in the afternoon   (f) e_{rms} in the afternoon

Figure 14: Comparisons of the statistics of the proposed analytical model and the HFLCAL model in terms of e_{power}, e_{peak} and e_{rms} for the selected heliostats (Table 3) in the midday and the late afternoon.

8. Conclusion

In this paper, a novel analytical model with a closed-form expression is proposed to describe the flux density distribution on the receiver plane that is reflected by a flat heliostat. The model takes various factors like sun, heliostat, atmosphere into account comprehensively, as well as the shadowing and blocking effects. It is the first convolution model with a closed-form expression for flux spot simulation. Experimental results and comparisons show that the proposed model is accurate. Due to its close-form expression, the model can be evaluated efficiently in parallel on a common desktop graphics processing unit. It takes only 2.8 milliseconds to generate a flux density distribution on the receiver plane. Since flux density distribution computation is one of the most fundamental operations for flux simulation of the whole field, heliostat field layout optimization and aiming strategy optimization in a central receiver system, the proposed model will greatly facilitate the related simulation and optimizations potentially.

Acknowledgements

Conflicts of interest

There are no conflicts of interest to declare.

Appendix

Appendix A. Expression of $f_i(0)$ and $f_i(1)$

According to (17), $f_i(0)$ and $f_i(1)$ are

$$
\begin{cases}
f_i(0) = \dfrac{1}{4}b_i\left(\dfrac{2S_4\sqrt{S_1}\arctan(S_9/\sqrt{S_1})}{b_i m S_2} + 2b_i S_3\dfrac{\arctan(S_9/\sqrt{S_1})}{\sqrt{S_1}S_2}\right. \\
\qquad\left. + \dfrac{2(-y+y_i)\arctan(\frac{-x+x_i}{\sqrt{m+(-y+y_i)^2}})}{b_i m\sqrt{m+(-y+y_i)^2}} + a_i\dfrac{\log(S_{11})}{S_2} - a_i\dfrac{\log(b_i^2 S_{11})}{S_2}\right) \\
f_i(1) = \dfrac{1}{4}b_i\left(\dfrac{2S_4\sqrt{S_1}\arctan(S_{10}/\sqrt{S_1})}{b_i m S_2} + 2b_i S_3\dfrac{\arctan(S_{10}/\sqrt{S_1})}{\sqrt{S_1}S_2}\right. \\
\qquad\left. + \dfrac{2(b_i-y+y_i)\arctan(\frac{a_i-x+x_i}{\sqrt{m+(b_i-y+y_i)^2}})}{b_i m\sqrt{m+(b_i-y+y_i)^2}} + a_i\dfrac{\log(S_{12})}{S_2}\right. \\
\qquad\left. - a_i\dfrac{\log(b_i^2 S_{12})}{S_2}\right)
\end{cases}
\tag{A.1}
$$

in which

$$
\begin{cases}
S_1 = b_i^2(m+(x-x_i)^2) + a_i^2(m+(y-y_i)^2) - 2a_i b_i(x-x_i)(y-y_i) \\
S_2 = b_i^2(x-x_i)^2 + a_i^2(m+(y-y_i)^2) - 2a_i b_i(x-x_i)(y-y_i) \\
S_3 = b_i(x-x_i) + a_i(-y+y_i) \\
S_4 = b_i(-x+x_i) + a_i(y-y_i)
\end{cases}
$$

$$
\begin{cases}
S_9 = a_i(-x+x_i) + b_i(-y+y_i) \\
S_{10} = a_i^2 + a_i(-x+x_i) + b_i(b_i-y+y_i) \\
S_{11} = m + (x-x_i)^2 + (y-y_i)^2 \\
S_{12} = m + (a_i-(x-x_i))^2 + (b_i-(y-y_i))^2 \\
m = 1/s^2
\end{cases}
$$

Appendix B. Oblique parallel projection equation

In the global coordinate system, suppose that $\boldsymbol{R} = (R_x, R_y, R_z)$ is a point on the receiver surface and that $\boldsymbol{H} = (H_x, H_y, H_z)$ is the corresponding point on the investigated heliostat surface under parallel projection along the reflection direction $\mathbf{r} = (r_x, r_y, r_z)$. $\boldsymbol{o}$ and $\boldsymbol{N}$ are the heliostat center and normal, respectively. Thus, $\boldsymbol{N}\cdot\boldsymbol{r}\neq 0$. The analytical relationship between $\boldsymbol{R}$ and $\boldsymbol{H}$ can be derived as follows.

According to the ray-plane intersection equation

$$
\begin{cases}
(\boldsymbol{H}-\boldsymbol{o})\cdot\boldsymbol{N} = 0 & \cdots \quad \text{Heliostat surface equation} \\
\boldsymbol{H}+t\boldsymbol{r} = \boldsymbol{R} & \cdots \qquad\qquad \text{Ray equation}
\end{cases}
\tag{B.1}
$$

we have

$$
t = \frac{\boldsymbol{N}\cdot(\boldsymbol{R}-\boldsymbol{o})}{\boldsymbol{N}\cdot\boldsymbol{r}}.
\tag{B.2}
$$

Substituting B.2 into the ray equation of B.1, we obtain

$$
\boldsymbol{H} = \boldsymbol{R} + \frac{\boldsymbol{N}\cdot(\boldsymbol{o}-\boldsymbol{R})}{\boldsymbol{N}\cdot\boldsymbol{r}}\boldsymbol{r}.
\tag{B.3}
$$

21

This expression can be rewritten in coordinate form with $a = \boldsymbol{N} \cdot \boldsymbol{r}$ and $b = \boldsymbol{N} \cdot \boldsymbol{o}$:

$$
\begin{cases}
H_x = & (1 - \dfrac{N_x r_x}{a})R_x & -\dfrac{N_y r_x}{a}R_y & -\dfrac{N_z r_x}{a}R_z & +\dfrac{b}{a}r_x \\[2mm]
H_y = & -\dfrac{N_x r_y}{a}R_x & +(1 - \dfrac{N_y r_y}{a})R_y & -\dfrac{N_z r_y}{a}R_z & +\dfrac{b}{a}r_y \\[2mm]
H_z = & -\dfrac{N_x r_z}{a}R_x & -\dfrac{N_y r_z}{a}R_y & +(1 - \dfrac{N_z r_z}{a})R_z & +\dfrac{b}{a}r_z
\end{cases}
\tag{B.4}
$$

Therefore,

$$
\boldsymbol{H} = \mathbf{M}\boldsymbol{R} + \frac{b}{a}\boldsymbol{r},
\tag{B.5}
$$

in which

$$
\mathbf{M} =
\begin{bmatrix}
1 - \frac{N_x r_x}{a} & -\frac{N_y r_x}{a} & -\frac{N_z r_x}{a} \\[2mm]
-\frac{N_x r_y}{a} & 1 - \frac{N_y r_y}{a} & -\frac{N_z r_y}{a} \\[2mm]
-\frac{N_x r_z}{a} & -\frac{N_y r_z}{a} & 1 - \frac{N_z r_z}{a}
\end{bmatrix}
= \mathbf{I} - \frac{1}{a}\boldsymbol{r}^{\mathrm{T}}\boldsymbol{N}.
\tag{B.6}
$$

References

Avila-Marin, A.L., Fernandez-Reche, J., Tellez, F.M., 2013. Evaluation of the potential of central receiver solar power plants: Configuration, optimization and trends. Applied Energy 112, 274–288. doi:`10.1016/j.apenergy.2013.05.049`.

Belhomme, B., Pitz-Paal, R., Schwarzbözl, P., Ulmer, S., 2009. A new fast ray tracing tool for high-precision simulation of heliostat fields. Journal of Solar Energy Engineering volume 131, 376–385. doi:`10.1115/1.3139139`.

Bendt, P., Rabl, A., 1981. Optical analysis of point focus parabolic radiation concentrators. Applied optics 20, 674–683. doi:`10.1364/AO.20.000674`.

Besarati, S.M., Goswami, D.Y., Stefanakos, E.K., 2014. Optimal heliostat aiming strategy for uniform distribution of heat flux on the receiver of a solar power tower plant. Energy Conversion and Management 84, 234–243. doi:`10.1016/j.enconman.2014.04.030`.

Biggs, F., Vittitoe, C.N., 1976. The helios model for the optical behavior of reflecting solar concentrators. Sandia National Laboratories Report Report N0.SAND76-0347 .

Blanco, M.J., Amieva, J.M., Mancillas, A., 2005. The tonatiuh software development project: An open source approach to the simulation of solar concentrating systems, in: ASME 2005 International Mechanical Engineering Congress and Exposition, American Society of Mechanical Engineers. pp. 157–164.

Boolean Operations on Polygons, 2016. URL: `https://en.wikipedia.org/wiki/Boolean_operations_on_polygons`. [Online; accessed 6-August-2018].

Buck, R.C., 2003. Advanced calculus. Waveland Press.

Buie, D., Monger, A., Dey, C., 2003. Sunshape distributions for terrestrial solar simulations. Solar Energy 74, 113–122. doi:`10.1016/S0038-092X(03)00125-7`.

Cádiz, P., Frasquet, M., Silva, M., Martínez, F., Carballo, J., 2015. Shadowing and blocking effect optimization for a variable geometry heliostat field. Energy Procedia 69, 60–69. doi:`10.1016/j.egypro.2015.03.008`.

Catmull, E., 1974. A Subdivision Algorithm for Computer Display of Curved Surfaces. Ph.D. thesis.

Chen, Y.T., Kribus, A., Lim, B.H., Lim, C.S., Chong, K.K., Karni, J., Buck, R., Pfahl, A., Bligh, T.P., 2004. Comparison of two sun tracking methods in the application of a heliostat field. Journal of Solar Energy Engineering 126, 638–644. doi:`10.1115/1.1634583`.

Collado, F., Gomez, A., Turégano, J., 1986. An analytic function for the flux density due to sunlight reflected from a heliostat. Solar Energy 37, 215–234. doi:`10.1016/0038-092X(86)90078-2`.

Collado, F.J., 2010. One-point fitting of the flux density produced by a heliostat. Solar Energy 84, 673–684. doi:`10.1016/j.solener.2010.01.019`.

Coordinate Systems (Direct3D), 2016. URL: `https://msdn.microsoft.com/en-us/library/windows/desktop/bb204853(v=vs.85).aspx`. [Online; accessed 6-August-2018].

Cruz, N.C., Salhi, S., Redondo, J.L., lvarez, J., Berenguel, M., Ortigosa, P.M., 2018. Hector, a new methodology for continuous and pattern-free heliostat field optimization. Applied Energy 225. doi:`10.1016/j.apenergy.2018.05.072`.

Duan, X., He, C., Zhao, Y., Feng, J., 2019. Quasi-Monte Carlo ray tracing: An efficient and accurate flux density distribution simulation method implemented on a GPU. To be submitted. .

Elsayed, M., Fathalah, K., 1994. Solar flux density distribution using a separation of variables/superposition technique. Renewable Energy 4, 77–87. doi:10.1016/0960-1481(94)90067-1.

Elsayed, M.M., Fathalah, K.A., Al-Rabghi, O.M., 1995. Measurements of solar flux density distribution on a plane receiver due to a flat heliostat. Solar Energy 54, 403–411. doi:10.1016/0038-092X(95)00010-0.

Fujimoto, A., Tanaka, T., Iwata, K., 1986. Arts: Accelerated ray-tracing system. IEEE Computer Graphics & Applications 6, 16–26. doi:10.1109/MCG.1986.276715.

García, L., Burisch, M., Sanchez, M., 2015. Spillage estimation in a heliostats field for solar field optimization. Energy Procedia 69, 1269–1276. doi:10.1016/j.egypro.2015.03.156.

García, P., Ferrière, A., Bezian, J.J., 2008. Codes for solar flux calculation dedicated to central receiver system applications: A comparative review. Solar Energy 82, 189–197. doi:10.1016/j.solener.2007.08.004.

He, C., Feng, J., Zhao, Y., 2017. Fast flux density distribution simulation of central receiver system on GPU. Solar Energy 144, 424–435. doi:10.1016/j.solener.2017.01.025.

Hennet, J., Abatut, J., 1984. An analytical method for reflected flux density calculations. Solar Energy 32, 357–363. doi:10.1016/0038-092X(84)90279-2.

Huang, W., Sun, L., 2016. Solar flux density calculation for a heliostat with an elliptical gaussian distribution source. Applied Energy 182, 434–441. doi:10.1016/j.apenergy.2016.08.082.

Kessenich, J., Sellers, G., Shreiner, D., 2016. OpenGL Programming Guide: The Official Guide to Learning OpenGL Version 4.5 (9th edition.). Addison-Wesley.

Kim, S., Lee, I., Lee, B.J., 2017. Development of performance analysis model for central receiver system and its application to pattern-free heliostat layout optimization. Solar Energy 153, 499–507. doi:10.1016/j.solener.2017.05.093.

Landman, W.A., Grobler, A., Gauché, P., Dinter, F., 2016. Incidence angle effects on circular gaussian flux density distributions for heliostat imaging. Solar Energy 126, 156–167. doi:10.1016/j.solener.2015.12.008.

Leary, P.L., Hankins, J.D., Hankins, J.D., 1979. A User's guide for MIRVAL: a computer code for comparing designs of heliostat-receiver optics for central receiver solar power plants. Technical Report Sandia Laboratories Report, Albuquerque, NM, Report No. SAND77-8280.

Lipps, F., Vant-Hull, L., 1978. A cellwise method for the optimization of large central receiver systems. Solar Energy 20, 505–516. doi:10.1016/0038-092X(78)90067-1.

Lipps, F., Walzel, M., 1978. An analytic evaluation of the flux density due to sunlight reflected from a flat mirror having a polygonal boundary. Solar Energy 21, 113–121. doi:10.1016/0038-092X(78)90038-5.

Lovegrove, K., Stein, W., 2012. Concentrating solar power technology: principles, developments and applications. Elsevier.

McCool, M., Fiume, E., 1992. Hierarchical poisson disk sampling distributions, in: Proceedings of the conference on Graphics interface, pp. 94–105.

McCormack, J., Sherstyuk, A., 1998. Creating and rendering convolution surfaces, in: Computer Graphics Forum, Wiley Online Library. pp. 113–120. doi:`10.1111/1467-8659.00232`.

Neumann, A., Witzke, A., Jones, S.A., Schmitt, G., 2002. Representative terrestrial solar brightness profiles, in: ASME Solar 2002: International Solar Energy Conference, American Society of Mechanical Engineers. pp. 325–333. doi:`10.1115/SED2002-1069`.

Osuna, R., Fernandez, V., Romero, S., 2004. PS10: a 11.0-mw solar tower power plant with saturated steam receiver, in: Proceedings of the 12th Solar PACES International Symposium on Concentrated Solar Power and Chemical Energy Technologies, Oaxaca, México.

Ramos, A., Ramos, F., 2014. Heliostat blocking and shadowing efficiency in the video-game era. arXiv preprint arXiv:1402.1690.2014 .

Roldn, M.I., Monterreal, R., 2014. Heat flux and temperature prediction on a volumetric receiver installed in a solar furnace. Applied Energy 120, 65–74. doi:`j.apenergy.2014.01.029`.

Romero, M., Steinfeld, A., 2012. Concentrating solar thermal power and thermochemical fuels. Energy & Environmental Science 5, 9234–9245. doi:`10.1039/C2EE21275G`.

Salomé, A., Chhel, F., Flamant, G., Ferrire, A., Thiery, F., 2013. Control of the flux distribution on a solar tower receiver using an optimized aiming point strategy: Application to themis solar tower. Solar Energy 94, 352–366. doi:`10.1016/j.solener.2013.02.025`.

Schell, S., 2011. Design and evaluation of esolars heliostat fields. Solar Energy 85, 614–619. doi:`10.1016/j.solener.2010.01.008`.

Schwarzbözl, P., Pitz-Paal, R., Schmitz, M., 2009. Visual HFLCAL - a software tool for layout and optimisation of heliostat fields, in: Proceedings of 15th International SolarPACES Symposium, pp. 15–18.

Soltrace project, 2018. URL: `https://github.com/NREL/SolTrace`. [Online; accessed 9-March-2019].

Tonatiuh project, 2018. URL: `https://github.com/iat-cener/tonatiuh`. [Online; accessed 9-March-2019].

Walzel, M., Lipps, F., Vant-Hull, L., 1977. A solar flux density calculation for a solar tower concentrator using a two-dimensional hermite function expansion. Solar Energy 19, 239–253. doi:`10.1016/0038-092X(77)90067-6`.

Wang, K., He, Y.L., Xue, X.D., Du, B.C., 2017. Multi-objective optimization of the aiming strategy for the solar power tower with a cavity receiver by using the non-dominated sorting genetic algorithm. Applied Energy 205, 399416. doi:`10.1016/j.apenergy.2017.07.096`.

Weiler, K., Atherton, P., 1977. Hidden surface removal using polygon area sorting, in: ACM SIGGRAPH Computer Graphics, ACM. pp. 214–222. doi:`10.1145/563858.563896`.

Weiler Clip Library, 2015. URL: `https://github.com/barak/clippoly`. [Online; accessed 6-August-2018].

Wendelin, T., 2003. Soltrace: A new optical modeling tool for concentrating solar optics, in: ASME 2003 International Solar Energy Conference, pp. 253–260.